Supplemental Material for
Stabilizing Even-Parity Chiral Superconductivity in Sr$_2$RuO$_4$

Han Gyeol Suh, Henri Menke, P. M. R. Brydon, Carsten Timm, Aline Ramires, and Daniel F. Agterberg

MICROSCOPIC MODEL

In this section, we construct a 3D tight-binding model for Sr$_2$RuO$_4$. We take into account the full 3D Fermi surfaces (FSs) of Sr$_2$RuO$_4$, based on the DFT band structure obtained by Veenstra et $al.$ [S1], who showed that despite the 2D shape of the FSs, the orbital and spin polarization vary along k_z. To account for the presence of orbital mixing on the different FS sheets, we include the t_{2g} manifold of the Ru d_{yz}, d_{xz}, and d_{xy} orbitals (we will assume this order throughout).

We parametrize the orbital space by the the Gell-Mann matrices, which are the generators of SU(3). We use the convention

$$
\lambda_0 = \begin{pmatrix} 1 & 0 & 0 \\ 0 & 1 & 0 \\ 0 & 0 & 1 \end{pmatrix}, \quad
\lambda_1 = \begin{pmatrix} 0 & 1 & 0 \\ 1 & 0 & 0 \\ 0 & 0 & 0 \end{pmatrix}, \quad
\lambda_2 = \begin{pmatrix} 0 & 0 & 1 \\ 0 & 0 & 0 \\ 1 & 0 & 0 \end{pmatrix}, \quad
\lambda_3 = \begin{pmatrix} 0 & 0 & 0 \\ 0 & 0 & 1 \\ 0 & 1 & 0 \end{pmatrix}, \quad
\lambda_4 = \begin{pmatrix} 0 & -i & 0 \\ i & 0 & 0 \\ 0 & 0 & 0 \end{pmatrix},
$$
$$
\lambda_5 = \begin{pmatrix} 0 & 0 & -i \\ 0 & 0 & 0 \\ i & 0 & 0 \end{pmatrix}, \quad
\lambda_6 = \begin{pmatrix} 0 & 0 & 0 \\ 0 & 0 & -i \\ 0 & i & 0 \end{pmatrix}, \quad
\lambda_7 = \begin{pmatrix} 1 & 0 & 0 \\ 0 & -1 & 0 \\ 0 & 0 & 0 \end{pmatrix}, \quad
\lambda_8 = \frac{1}{\sqrt{3}} \begin{pmatrix} 1 & 0 & 0 \\ 0 & 1 & 0 \\ 0 & 0 & -2 \end{pmatrix}.
$$
(1)

We write the normal-state Hamiltonian in terms of the spinor $\Phi_{\boldsymbol{k}} = (c_{\boldsymbol{k},2,\uparrow}, c_{\boldsymbol{k},2,\downarrow}, c_{\boldsymbol{k},1,\uparrow}, c_{\boldsymbol{k},1,\downarrow}, c_{\boldsymbol{k},3,\uparrow}, c_{\boldsymbol{k},3,\downarrow})^T$, where we introduce the numbering of the orbitals $1 = d_{xz}$, $2 = d_{yz}$, $3 = d_{xy}$. In terms of the Gell-Mann and Pauli matrices, we write the Hamiltonian $H_0 = \sum_{\boldsymbol{k}} \Phi_{\boldsymbol{k}}^\dagger \hat{H}_0(\boldsymbol{k}) \Phi_{\boldsymbol{k}}$ where

$$
\hat{H}_0(\boldsymbol{k}) = \sum_{a,b} h_{ab}(\boldsymbol{k})\, \lambda_a \otimes \sigma_b.
$$
(2)

In the presence of inversion and time-reversal symmetries, only a subset of fifteen $h_{ab}(\boldsymbol{k})$ terms are allowed. Table I lists the symmetry-allowed terms, the associated irrep for the matrices $\lambda_a \otimes \sigma_b$, the physical process to which these correspond, and their momentum dependence.

Irrep	(a,b)	Type	Explicit form of $h_{ab}(\boldsymbol{k})$
A_{1g}	$(0,0)$	intra-orbital hopping	$\frac{1}{3}\left[\xi_{11}(\boldsymbol{k}) + \xi_{22}(\boldsymbol{k}) + \xi_{33}(\boldsymbol{k})\right]$
	$(8,0)$	intra-orbital hopping	$\frac{1}{2\sqrt{3}}\left[\xi_{11}(\boldsymbol{k}) + \xi_{22}(\boldsymbol{k}) - 2\xi_{33}(\boldsymbol{k})\right]$
	$(4,3)$	atomic SOC	$-\eta_z$
	$(5,2)-(6,1)$	atomic-SOC	$\eta_\perp$
A_{2g}	$(5,1)+(6,2)$	$\boldsymbol{k}$-SOC	neglected
B_{1g}	$(7,0)$	intra-orbital hopping	$\frac{1}{2}\left[\xi_{22}(\boldsymbol{k}) - \xi_{11}(\boldsymbol{k})\right]$
	$(5,2)+(6,1)$	$\boldsymbol{k}$-SOC	$2t_{5261}^{\mathrm{SOC}}(\cos k_x a - \cos k_y a)$
B_{2g}	$(1,0)$	inter-orbital hopping	$\lambda(\boldsymbol{k})$
	$(5,1)-(6,2)$	$\boldsymbol{k}$-SOC	$4t_{5162}^{\mathrm{SOC}} \sin k_x a \sin k_y a$
E_g	$\{(2,0),(3,0)\}$	inter-orbital hopping	$8t_z^{13}\sin(k_z c/2)\{\sin(k_x a/2)\cos(k_y a/2), \cos(k_x a/2)\sin(k_y a/2)\}$
	$\{(4,1),(4,2)\}$	$\boldsymbol{k}$-SOC	$8t_{12z}^{\mathrm{SOC}}\sin(k_z c/2)\{\sin(k_x a/2)\cos(k_y a/2), \cos(k_x a/2)\sin(k_y a/2)\}$
	$\{(6,3),-(5,3)\}$	$\boldsymbol{k}$-SOC	$-8t_{56z}^{\mathrm{SOC}}\sin(k_z c/2)\{\sin(k_x a/2)\cos(k_y a/2), \cos(k_x a/2)\sin(k_y a/2)\}$

TABLE I. List of the fifteen symmetry-allowed terms in the normal-state Hamiltonian $\hat{H}_0(\boldsymbol{k})$ in Eq. (2). For each (a,b), the basis function $h_{ab}(\boldsymbol{k})$ must belong to the same irrep of D_{4h} as the matrix $\lambda_a \otimes \sigma_b$. The table gives the irrep, the associated physical process ("Type"), where "$\boldsymbol{k}$-SOC" means momentum-dependent (nonlocal) SOC, and the momentum dependence of $h_{ab}(\boldsymbol{k})$. For the two-dimensional irrep E_g, the entries are organized such that the first transforms as xz and the second as yz.

Note that Table I has entries which are in accordance with previous literature [S2, S3, S4] but there are also new terms associated with hopping along the z-direction or momentum-dependent SOC, which are usually neglected. Here we take $\eta_z = \eta_\perp = \eta$ as the parameter for the on-site atomic SOC. The intra-orbital hoppings $\xi_{11,22,33}(\boldsymbol{k})$ are included up to next-next-nearest neighbors in plane and next-nearest neighbors out of plane. The inter-orbital hopping $\lambda(\boldsymbol{k})$ between the d_{xz} and the d_{yz} orbitals is kept up to next-nearest neighbors in plane and nearest neighbors out of plane. For the inter-orbital hopping $\{(3,0), -(2,0)\}$ between the d_{xz} and d_{xy} (d_{yz} and d_{xy}) orbitals, we only keep the nearest-neighbor component out of plane. The explicit form of the functions not given explicitly in Table I is

$$
\begin{aligned}
\xi_{11,22}(\boldsymbol{k}) = {}& 2t^{11}_{x,y}\cos k_x a + 2t^{11}_{y,x}\cos k_y a \\
& + 8t^{11}_z \cos(k_x a/2)\cos(k_y a/2)\cos(k_z c/2) \\
& + 4t^{11}_{xy}\cos k_x a\cos k_y a + 2t^{11}_{xx,yy}\cos 2k_x a + 2t^{11}_{yy,xx}\cos 2k_y a \\
& + 4t^{11}_{xxy,xyy}\cos 2k_x a\cos k_y a + 4t^{11}_{xyy,xxy}\cos 2k_y a\cos k_x a \\
& + 2t^{11}_{zz}(\cos k_z c - 1) - \mu,
\end{aligned}
\tag{3}
$$

$$
\begin{aligned}
\xi_{33}(\boldsymbol{k}) = {}& 2t^{33}_x(\cos k_x a + \cos k_y a) \\
& + 8t^{33}_z \cos(k_x a/2)\cos(k_y a/2)\cos(k_z c/2) \\
& + 4t^{33}_{xy}\cos k_x a\cos k_y a + 2t^{33}_{xx}(\cos 2k_x a + \cos 2k_y a) \\
& + 4t^{33}_{xxy}(\cos 2k_x a\cos k_y a + \cos 2k_y a\cos k_x a) \\
& + 2t^{33}_{zz}(\cos k_z c - 1) - \mu_1,
\end{aligned}
\tag{4}
$$

$$
\begin{aligned}
\lambda(\boldsymbol{k}) = {}& 4t^{12}_z \sin(k_x a/2)\sin(k_y a/2)\cos(k_z c/2) \\
& - 4t^{12}_{xy}\sin k_x a\sin k_y a \\
& - 4t^{12}_{xxy}(\sin 2k_x a\sin k_y a + \sin 2k_y a\sin k_x a).
\end{aligned}
\tag{5}
$$

We now focus on terms corresponding to $\boldsymbol{k}$-dependent SOC, usually not taken into account in the standard parametrization of the normal-state Hamiltonian. The first matrix in the list, $\lambda_5 \otimes \sigma_1 + \lambda_6 \otimes \sigma_2$, which is of A_{2g} symmetry, will be ignored because the lowest-order polynomial basis function of this irrep is of order 4 (g-wave), which only appears at next-next-next-nearest-neighbor hopping and is therefore assumed to be negligible. We also take the other $\boldsymbol{k}$-dependent SOC terms at the lowest order at which they appear. This concludes the construction of the microscopic model, which is characterized by a Hamiltonian with 26 free parameters.

FIT TO DFT RESULTS

We employ the tight-binding model presented in the supplemental material of [S1] to determine the free parameters. The tight-binding Hamiltonian is derived from an LDA band structure that is down-folded onto the O-$2p$ and the Ru-$4d$ orbitals and therefore has a total of 17 bands. The hopping integrals are truncated at $10\,\text{meV}$. We henceforth refer to the LDA-derived tight-binding Hamiltonian as the "DFT model". For the calculation of the linearized gap equation, the DFT model is much too large and most of the bands are irrelevant for superconductivity. The states at the Fermi surface are determined by the t_{2g} manifold of the Ru-$4d$ orbitals (d_{yz}, d_{xz}, d_{xy}) and we fit Eq. (2) to several quantities extracted from the DFT model projected into this subspace.

We extract the Fermi momenta $\tilde{\boldsymbol{k}}_F$ of the DFT model and denote the eigenvalues by ϵ and the associated eigenvectors by V. We define the following measure

$$
S = \sum_{n=\alpha,\beta,\gamma,\,\tilde{\boldsymbol{k}}_F} \left[\left(\epsilon^n(\tilde{\boldsymbol{k}}_F)\right)^2 + \left(\tilde{d}^n_{xy}(\tilde{\boldsymbol{k}}_F) - d^n_{xy}(\tilde{\boldsymbol{k}}_F)\right)^2 + \left(\tilde{p}^n_{\text{SOC}}(\tilde{\boldsymbol{k}}_F) - p^n_{\text{SOC}}(\tilde{\boldsymbol{k}}_F)\right)^2 + \left(\tilde{v}^n_\parallel(\tilde{\boldsymbol{k}}_F) - v^n_\parallel(\tilde{\boldsymbol{k}}_F)\right)^2 \right],
\tag{6}
$$

where the sum is over momenta $\tilde{\boldsymbol{k}}_F$ on the DFT Fermi surfaces formed by the bands $n = \alpha, \beta, \gamma$, $\epsilon^n(\boldsymbol{k})$ are the band energies, $d^n_{xy}(\boldsymbol{k})$ is the d_{xy}-orbital content, $p^n_{\text{SOC}}(\boldsymbol{k})$ is the spin polarization, and $v^n_\parallel(\boldsymbol{k})$ the in-plane velocity. Quantities with a tilde are from the DFT model. The d_{xy}-orbital content is determined by the corresponding eigenvector components

$$
d^n_{xy}(\boldsymbol{k}) = \frac{1}{2}\left(|V^{n,\uparrow}_{d_{xy},\uparrow}(\boldsymbol{k})|^2 + |V^{n,\uparrow}_{d_{xy},\downarrow}(\boldsymbol{k})|^2 + |V^{n,\downarrow}_{d_{xy},\uparrow}(\boldsymbol{k})|^2 + |V^{n,\downarrow}_{d_{xy},\downarrow}(\boldsymbol{k})|^2 \right).
\tag{7}
$$

t_x^{11}	-362.4	t_y^{11}	-134	t_x^{33}	-262.4	t_{xy}^{11}	-44.01	t_{xx}^{11}	-1.021
t_{yy}^{11}	-5.727	t_{xy}^{33}	-43.73	t_{xx}^{33}	34.23	t_{xy}^{12}	16.25	t_{xxy}^{11}	-13.93
t_{xyy}^{11}	-7.52	t_{xxy}^{33}	8.069	t_{xxy}^{12}	3.94	η	57.39	μ	438.5
μ_1	218.6	t_z^{11}	-0.0228	t_z^{33}	1.811	t_z^{12}	19.95	t_z^{13}	8.304
t_{zz}^{11}	2.522	t_{zz}^{33}	-3.159	t_{56z}^{SOC}	-1.247	t_{12z}^{SOC}	-3.576	t_{5162}^{SOC}	-1.008
t_{5261}^{SOC}	0.3779								

TABLE II. Parameters of the Hamiltonian (2) determined from the fit to the DFT model. All values are in meV.

The spin polarization is determined from the expectation value of the atomic spin-orbit coupling Hamiltonian $H_{\mathrm{SOC}} = \lambda_5\sigma_2 - \lambda_6\sigma_1 - \lambda_4\sigma_3$:

$$p_{\mathrm{SOC}}^n(\boldsymbol{k}) = 1 + \left[\frac{1}{2}\,\mathrm{Re}\big(V^{n,\uparrow T}(\boldsymbol{k})H_{\mathrm{SOC}}V^{n,\uparrow}(\boldsymbol{k}) + V^{n,\downarrow T}(\boldsymbol{k})H_{\mathrm{SOC}}V^{n,\downarrow}(\boldsymbol{k})\big)\right]^{1/3}. \tag{8}$$

For the in-plane Fermi velocity we use a simple two-point central finite differences stencil where $\varepsilon_{x,y}$ are small

$$v_\parallel^n(\boldsymbol{k}) = \sqrt{\left|\frac{\epsilon^n(\boldsymbol{k}-\varepsilon_x) - \epsilon^n(\boldsymbol{k}+\varepsilon_x)}{2\varepsilon_x}\right|^2 + \left|\frac{\epsilon^n(\boldsymbol{k}-\varepsilon_y) - \epsilon^n(\boldsymbol{k}+\varepsilon_y)}{2\varepsilon_y}\right|^2}. \tag{9}$$

We minimize the measure (6) using the derivative-free optimization algorithm BOBYQA of dlib [S5].

The fit yields very good agreement with the DFT model close to the Fermi energy, including good reproduction of the d_{xy}-orbital content and the spin polarization. In Fig. 1, we compare the result of our fit with the DFT model in the $k_z = 0$ plane. In Fig. 2, we show the full 3D Fermi surface produced by our fit, together with the d_{xy}-orbital content and the spin polarization. The corresponding fit parameters are listed in Tab. II.

It is important to note that because the different sheets of the Fermi surface have varying orbital and spin content, it is not possible to isolate one dominant band for superconductivity. The pairing state will in general have contributions from all three sheets.

LINEARIZED GAP EQUATION

In this section, we outline our solution of the linearized BCS gap equation. For convenience, we repeat the second-order expansion of the free energy as given in Eq. (3) of the main text,

$$\mathcal{F} = \frac{1}{2}\sum_i \frac{1}{g_i}\,\mathrm{Tr}\,[\hat{\Delta}_i^\dagger\hat{\Delta}_i] - \frac{k_BT}{2}\sum_{\boldsymbol{k},\omega,i,j}\mathrm{Tr}\,[\hat{\Delta}_i\underline{\hat{G}}\hat{\Delta}_j^\dagger\hat{G}], \tag{10}$$

where the gap functions are $\hat{\Delta}_i = \Delta_i\,\lambda_{a_i}\otimes\sigma_{b_i}\,(i\sigma_2)$ and the indices a_i, b_i, and interaction energies g_i are given in Table 1 of the main text. We introduce an interaction scaling parameter s, and for concreteness choose the interaction energies to be given by $U = 5/s$, $U' = 1/s$, and $J = 2/s$. Since we are interested in the weak-coupling limit we will later assume s to be large. The Green's functions and gap function are expressed in the energy eigenbasis by

$$\hat{G} \rightarrow U^\dagger \hat{G} U = \mathrm{diag}\left(\frac{1}{i\omega_n - \epsilon_a}\right), \tag{11}$$

$$\underline{\hat{G}} \rightarrow \underline{U}^\dagger \underline{\hat{G}}\,\underline{U} = \mathrm{diag}\left(\frac{1}{i\omega_n + \epsilon_a}\right), \tag{12}$$

$$\hat{\Delta}_i \rightarrow U^\dagger \hat{\Delta}_i\,\underline{U}, \tag{13}$$

where U is a unitary matrix that diagonalizes the normal-state Hamiltonian $\hat{H}_0$, $\underline{U} = (i\sigma_2)^\dagger U$, and ϵ_a are band energies. We define new gap matrices by

$$\Lambda_i = U^\dagger\left(\lambda_{a_i}\otimes\sigma_{b_i}\right)U. \tag{14}$$

The frequency summation yields

$$S_{ab}(\boldsymbol{k},\beta) = -\frac{1}{\beta}\sum_{\omega_n}\frac{1}{i\omega_n - \epsilon_a}\frac{1}{i\omega_n + \epsilon_b} = \frac{1}{2}\frac{\tanh(\beta\epsilon_a/2) + \tanh(\beta\epsilon_b/2)}{\epsilon_a + \epsilon_b}, \tag{15}$$
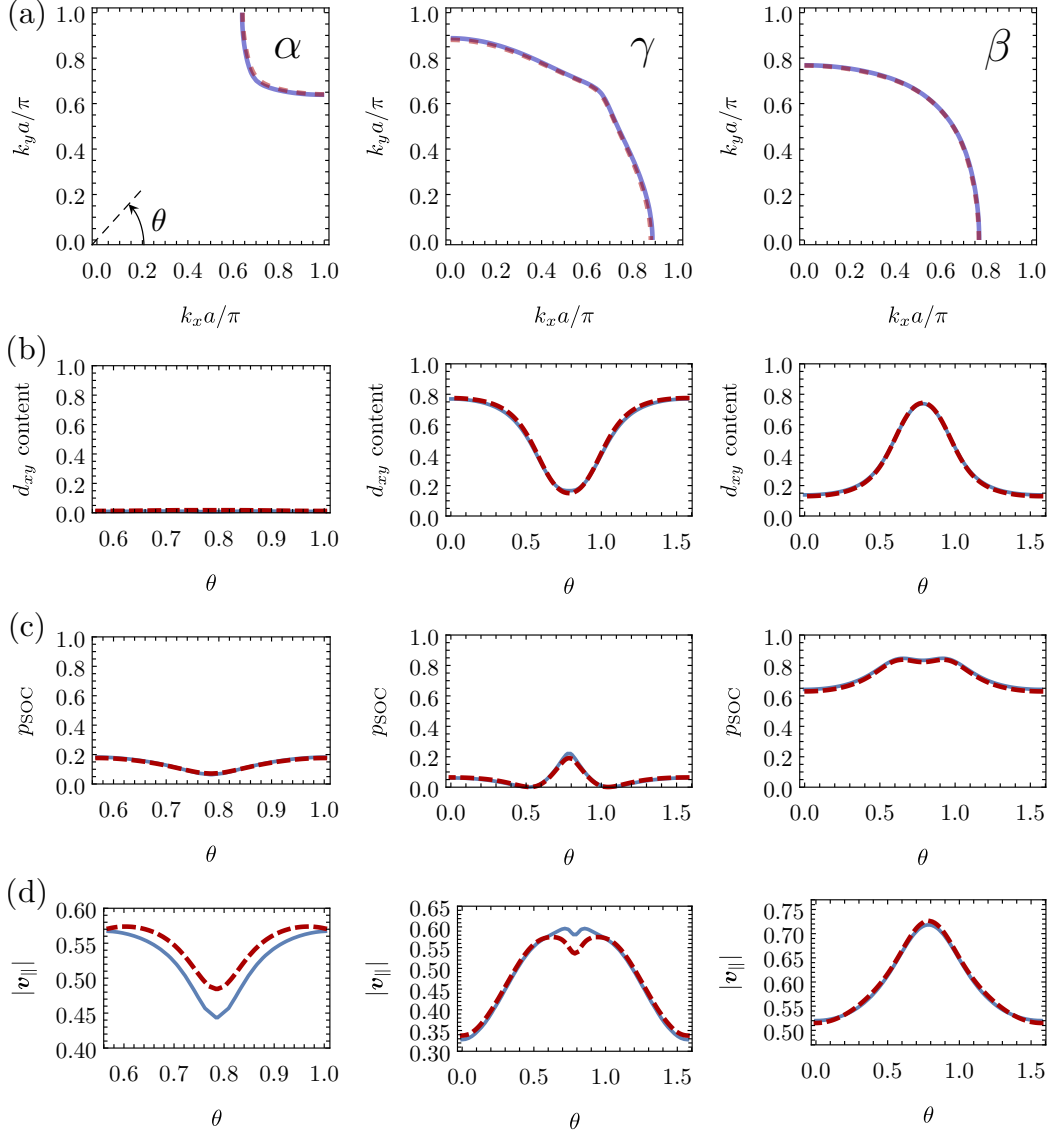
FIG. 1. Comparison of the DFT model (red dashed lines) with our fit (blue solid lines) in the $k_z = 0$ plane. (a) Fermi surface in the first quadrant of the Brillouin zone. (b) d_{xy}-orbital content, (c) spin polarization, and (d) in-plane velocity as functions of the angle $\theta = \arctan(k_y/k_x)$ in the first quadrant. The three columns pertain to the α, γ, and β band.

where $\beta = 1/k_B T$. The linearized gap equations are obtained by differentiating the free energy with respect to the gap amplitudes, $\partial \mathcal{F}/\partial \Delta_i^* = 0$, written explicitly as

$$\sum_j \left(s \frac{\delta_{ij}}{\tilde{g}_i} \text{Tr}\left[\Lambda_i^\dagger \Lambda_i\right] + \sum_{\boldsymbol{k},a,b} [\Lambda_i]_{ab}^* [\Lambda_j]_{ab} \, S_{ab} \right) \Delta_j = 0, \tag{16}$$

where i and j run over all gap-structure indices of a given irrep, a and b run over band indices, $[\Lambda_i]_{ab}$ is a matrix element of Λ_i, and $\tilde{g}_i$ is the value of g_i when $s = 1$.

First, consider $\epsilon_a = \epsilon_b$ intraband terms in Eq. (16), the $\boldsymbol{k}$-integration is written as

$$\sum_{\boldsymbol{k},\epsilon_a=\epsilon_b} [\Lambda_i]_{ab}^* [\Lambda_j]_{ab} \, S_{ab} = \sum_{\epsilon_a=\epsilon_b} \frac{1}{2} \int \mathrm{d}\epsilon \, F_{abij}(\epsilon) \frac{\tanh(\beta\epsilon/2)}{\epsilon}, \tag{17}$$
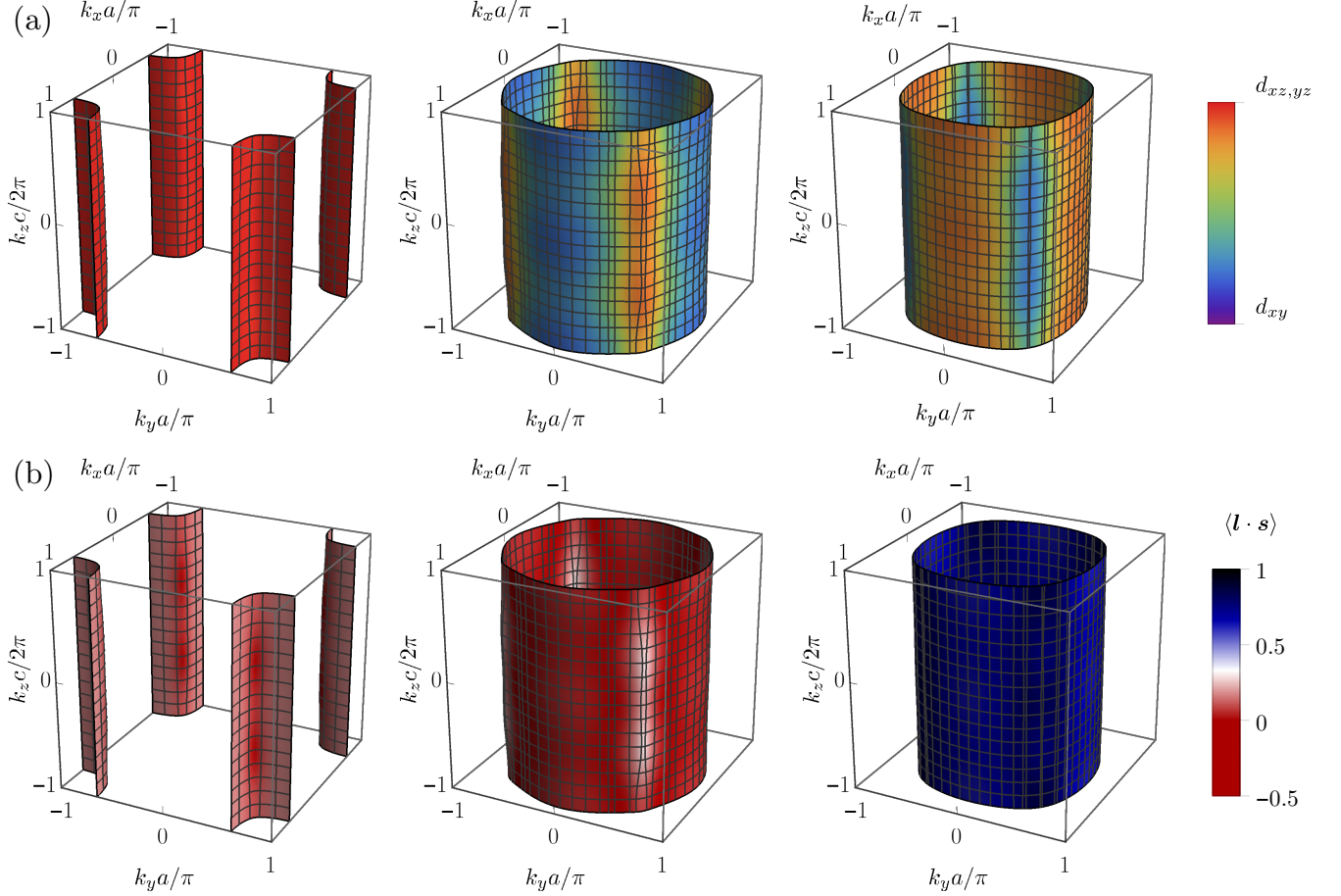
FIG. 2. Full 3D Fermi surface obtained from the best fit to the DFT results of Ref. [S1], with color indicating (a) the d_{xy}-orbital content and (b) the spin polarization. The three columns pertain to the α, γ, and β band.

with

$$F_{abij}(\epsilon) = \frac{1}{(2\pi)^3} \iint_{\epsilon_a(\boldsymbol{k})=\epsilon} \mathrm{d}^2\boldsymbol{k} \, \frac{\delta_{\epsilon_a \epsilon_b}}{\|\boldsymbol{\nabla}\epsilon_a\|} [\Lambda_i]^*_{ab} [\Lambda_j]_{ab}. \tag{18}$$

Use the Taylor expansion of $F_{abij}(\epsilon)$ around the Fermi level, $F_{abij}(0) + \epsilon F'_{abij}(0) + \ldots$, the derivative of Eq. (17) with respect to β gives

$$\frac{\partial}{\partial \beta} \sum_{\boldsymbol{k}, \epsilon_a = \epsilon_b} [\Lambda_i]^*_{ab} [\Lambda_j]_{ab} S_{ab} = \frac{1}{\beta} \sum_{\epsilon_a = \epsilon_b} F_{abij}(0) + O\left(\frac{1}{\beta^3}\right). \tag{19}$$

Note that when this is integrated with respect to β it yields the $\log \beta$ divergence in Eq. (17). Next, consider the $\epsilon_a \neq \epsilon_b$ interband terms, as $\beta \to \infty$, S_{ab} converges to $\theta(\epsilon_a \epsilon_b)/|\epsilon_a + \epsilon_b|$, where θ is the Heaviside step function. Because this is a bounded function, there is no divergence in the interband contributions. In Eq. (16) a non-trivial solution for the gap amplitudes Δ_j is found by considering i and j as matrix indices and taking the corresponding 6×6 matrix to be singular. Including both the intraband and interband contributions, the critical β_c satisfies

$$\det \left[s \frac{\delta_{ij}}{\tilde{g}_i} \mathrm{Tr}\,[\Lambda_i^\dagger \Lambda_i] + \log \beta_c \sum_{\epsilon_a = \epsilon_b} F_{abij}(0) + C_{ij}(\beta_c) \right] = 0, \tag{20}$$

where $C_{ij}(\beta)$ is the portion of $\sum_{\boldsymbol{k},a,b} [\Lambda_i]^*_{ab} [\Lambda_j]_{ab} S_{ab}$ that remains after removing the $\log \beta$ divergent term. By definition, $C_{ij}(\beta)$ is convergent as $\beta \to \infty$, so the last term in the determinant can be ignored when s is sufficiently large. More explicitly, in the weak-coupling limit $s \to \infty$, T_c is given in the form

$$\log T_c(s) \approx -ms + \delta, \tag{21}$$

where δ is a constant and m is the smallest $\log \beta_c/s$ solution found when $C_{ij} = 0$.

Different channels (irreps) have different values of m, and the channel with the smallest m is the leading instability in the weak-coupling limit. Note that the definition of m does not depend on C_{ij} and all the interband contributions go into C_{ij}. Thus we can drop the interband terms in Eq. (16). This changes δ but does not change m. The resultant expression is

$$\det \left[s \frac{\delta_{ij}}{\tilde{g}_i} \text{Tr} \left[\Lambda_i^\dagger \Lambda_i \right] + \sum_{\boldsymbol{k}, \epsilon_a = \epsilon_b} [\Lambda_i]_{ab}^* [\Lambda_j]_{ab} \, S_{ab} \right] = 0, \tag{22}$$

which is the equation we solve numerically. The $\log \beta$ divergence originates from momenta near the Fermi surface, so we carry out the $\boldsymbol{k}$-integration on adaptive meshes with finer resolution near the Fermi surface. We obtain $\log \beta_c$ for several values of s and use linear regression to get the slope, which determines m. If the values of $\log \beta_c$ at the sampling points are not linear in s we sample larger s values until we encounter linear behavior. In our calculation, an equidistant set of four sampling points is used for a linear regression and their R^2 measures are always greater than 0.999. Using this procedure, we get the slope m for each pairing channel and determine the leading instability at each point in the phase diagram displayed in Fig. 1(a) in the main text. While this procedure may seem more elaborate than a direct solution of Eq. (20) with $C_{ij} = 0$, it allows us to verify Eq. (21) showing that our solution is in the weak coupling limit.

SUPERCONDUCTING-FITNESS ANALYSIS

In this section, we present details of the superconducting-fitness analysis. We start with the more realistic three-orbital model and then consider an effective two-orbital model, which dramatically simplifies the analysis but gives consistent results.

Complete 3D three-orbital model

In previous works [S6, S7], a proof of the direct relation between the superconducting-fitness measures $\hat{F}_C(\boldsymbol{k})$ and $\hat{F}_A(\boldsymbol{k})$ (defined below) and the superconducting critical temperature was provided for the one- and two-orbital scenario. The first measure,

$$\hat{F}_C(\boldsymbol{k}) = \tilde{H}_0(\boldsymbol{k})\tilde{\Delta}(\boldsymbol{k}) - \tilde{\Delta}(\boldsymbol{k})\tilde{H}_0^*(-\boldsymbol{k}), \tag{23}$$

quantifies how incompatible a given gap structure is for a specific normal state, namely, how much inter-band pairing there is. Here, $\tilde{H}_0(\boldsymbol{k}) = \hat{H}_0(\boldsymbol{k}) - h_{00}(\boldsymbol{k})\,\lambda_0 \otimes \sigma_0$ and we have defined a normalized gap matrix $\tilde{\Delta}(\boldsymbol{k}) = \hat{\Delta}(\boldsymbol{k})/|\hat{\Delta}(\boldsymbol{k})|$ such that average over the normal-state Fermi surface is $\langle \tilde{\Delta}(\boldsymbol{k})\tilde{\Delta}^\dagger(\boldsymbol{k}) \rangle_{\text{FS}} = \mathbb{1}$. The second measure,

$$\hat{F}_A(\boldsymbol{k}) = \tilde{H}_0(\boldsymbol{k})\tilde{\Delta}(\boldsymbol{k}) + \tilde{\Delta}(\boldsymbol{k})\tilde{H}_0^*(-\boldsymbol{k}), \tag{24}$$

quantifies how much intra-band pairing there is, or what fraction of the gap survives upon projection onto the Fermi surface. For the two-orbital scenario, these measures satisfy $\langle \text{Tr}\, \hat{F}_A^\dagger(\boldsymbol{k})\hat{F}_A(\boldsymbol{k}) + \text{Tr}\, \hat{F}_C^\dagger(\boldsymbol{k})\hat{F}_C(\boldsymbol{k}) \rangle_{\text{FS}} = 1$, up to normalization of the normal-state Hamiltonian, which highlights their complementarity. The proof of this relation relies on the fact that the matrices associated with the orbital DOF are Pauli matrices for the two-orbital scenario and therefore form a totally anticommuting set, which greatly simplifies the calculations. On the other hand, for $n > 2$ orbitals, the basis matrices are the generators of $\text{SU}(n)$, which do not form a totally anticommuting set and therefore do not allow a direct generalization of this relation for models with more than two orbitals. However, the physical meaning of $\hat{F}_C(\boldsymbol{k})$ and $\hat{F}_A(\boldsymbol{k})$ is preserved within some approximations, as discussed below.

For the three-orbital situation, the corresponding superconducting-fitness functions can be identified as

$$\hat{F}_{A,C}^{3orb}(\boldsymbol{k}) = [\hat{H}_0(\boldsymbol{k})]^2 \tilde{\Delta}(\boldsymbol{k}) \pm \tilde{\Delta}(\boldsymbol{k})[\hat{H}_0^*(-\boldsymbol{k})]^2. \tag{25}$$

Given that $[A^2, B]_\pm = A[A, B] \mp [A, B]A$, the core of the analysis still depends on the original form of the superconducting-fitness functions. Therefore, we use the form linear in $\hat{H}_0(\boldsymbol{k})$ to get some insight. Below, we will see that a simplified two-orbital model, for which the linear version of the fitness functions is valid rigorously, corroborates our analysis. We summarize the results for the complete three-orbital problem in Tables III and IV. The first row

7

			A_{1g}			A_{2g}	B_{1g}		B_{2g}		E_g					
Irrep	$[a,b]$	Interac.	$\mathbf{h_{80}}$	$\mathbf{h_{43}}$	$\mathbf{h_{52-61}}$	h_{51+62}	$\mathbf{h_{70}}$	h_{52+61}	$\mathbf{h_{10}}$	h_{51-62}	h_{20}	h_{30}	h_{41}	h_{42}	h_{53}	h_{63}
A_{1g}	$[0,0]$	$U+2J'$	$\frac{32}{3}$	$\frac{32}{3}$	$\frac{64}{3}$	$\frac{128}{3}$	$\frac{32}{3}$	$\frac{128}{3}$	$\frac{32}{3}$	$\frac{64}{3}$	$\frac{32}{3}$	$\frac{32}{3}$	$\frac{32}{3}$	$\frac{32}{3}$	$\frac{32}{3}$	$\frac{32}{3}$
	$[8,0]$	$U-J'$	16	$\frac{16}{3}$	$\frac{8}{3}$	$\frac{16}{3}$	$\frac{16}{3}$	$\frac{16}{3}$	$\frac{16}{3}$	$\frac{8}{3}$	$\frac{4}{3}$	$\frac{4}{3}$	$\frac{16}{3}$	$\frac{16}{3}$	$\frac{4}{3}$	$\frac{4}{3}$
	$[4,3]$	$\mathbf{U'-J}$	$\frac{16}{3}$	16	8	16	0	16	0	8	4	4	0	0	4	4
	$[5,2]-[6,1]$	$\mathbf{U'-J}$	$\frac{5}{3}$	3	24	8	3	8	3	8	2	2	4	4	2	2
A_{2g}	$[5,1]+[6,2]$	$\mathbf{U'-J}$	$\frac{5}{3}$	3	0	32	3	32	3	8	2	2	4	4	2	2
B_{1g}	$[7,0]$	$U-J'$	$\frac{16}{3}$	0	8	16	16	16	0	8	4	4	0	0	4	4
	$[5,2]+[6,1]$	$\mathbf{U'-J}$	$\frac{5}{3}$	3	8	32	3	32	3	0	2	2	4	4	2	2
B_{2g}	$[1,0]$	$U'+J$	$\frac{16}{3}$	0	8	16	0	16	16	8	4	4	0	0	4	4
	$[5,1]-[6,2]$	$\mathbf{U'-J}$	$\frac{5}{3}$	3	8	8	3	8	3	24	2	2	4	4	2	2
E_g	$+[3,0]$	$U'+J$	$\frac{4}{3}$	4	4	8	4	8	4	4	4	16	4	4	4	0
	$-[2,0]$		$\frac{4}{3}$	4	4	8	4	8	4	4	16	4	4	4	0	4
E_g	$+[4,2]$	$\mathbf{U'-J}$	$\frac{16}{3}$	0	8	16	0	16	0	8	4	4	0	16	4	4
	$-[4,1]$		$\frac{16}{3}$	0	8	16	0	16	0	8	4	4	16	0	4	4
E_g	$+[5,3]$	$\mathbf{U'-J}$	$\frac{4}{3}$	4	4	8	4	8	4	4	0	4	4	4	16	4
	$+[6,3]$		$\frac{4}{3}$	4	4	8	4	8	4	4	4	0	4	4	4	16

TABLE III. Superconducting-fitness measure $\hat{F}_A$ for the 3D three-orbital model for Sr$_2$RuO$_4$. The first column gives the irreps of the order parameters associated with matrix form $[a,b]$ (second column) and the third column displays the local interaction in the respective channel, where the potentially attractive channels are highlighted in boldface. Columns 4–17 give the results for the fitness function such that $\mathrm{Tr}\,\hat{F}_A^\dagger \hat{F}_A = \sum_{cd}(\text{table entry})\,|h_{cd}|^2$, for each term h_{cd} in the normal-state Hamiltonian, indicated in the second row with the associated irrep given in the first row. We highlight in boldface the h_{cd} terms which are present in the standard 2D models for Sr$_2$RuO$_4$, while the terms in normal typeface are either momentum-dependent SOC or interlayer couplings.

gives the irrep of each term in the normal-state Hamiltonian displayed in the second row as h_{ab}. The first column gives the irrep of each order parameter displayed in the second column following the notation $[a,b]$ corresponding to $\hat{\Delta} = \lambda_a \otimes \sigma_b\,(i\sigma_2)$. The third column gives the interaction stemming from the Hubbard-Kanamori Hamiltonian for each channel. Finally, the numerical entries in the tables correspond to $\mathrm{Tr}\,\hat{F}_{A,C}^\dagger \hat{F}_{A,C} = \sum_{cd}(\text{table entry})\,|h_{cd}|^2$.

Note that the order parameters with a potentially attractive interaction $U'-J$ are $[4,3]$ and $[5,2]-[6,1]$ in A_{1g}, $[5,1]+[6,2]$ in A_{2g}, $[5,2]+[6,1]$ in B_{1g}, $[5,1]-[6,2]$ in B_{2g}, and finally $\{[4,2],-[4,1]\}$ and $\{[5,3],[6,3]\}$ in E_g. All these order parameters are associated with spin-triplet states. If we focus first on the largest terms in the normal-state Hamiltonian, namely h_{80} and h_{70} (intra-orbital hopping), h_{10} (inter-orbital hopping), and h_{43} and h_{52-61} (atomic SOC), we conclude from Tables III and IV that, among the one-dimensional irreps, the most stable state should be in the A_{1g} channel since these states are associated with larger entries for $\hat{F}_A$ and smaller entries for $\hat{F}_C$.

Considering now the two-dimensional order parameters, for $\{[4,2],-[4,1]\}$, we find that the terms stabilizing it, i.e., the ones with the largest contribution to $\hat{F}_A$, are h_{51+62}, h_{52+61}, and $\{h_{42},-h_{41}\}$, all associated with momentum-dependent SOC. However, these terms contribute with the same value to the detrimental fitness measure $\hat{F}_C$, suggesting that they overall do not favor this pairing state. On the other hand, the two-dimensional order parameter $\{[5,3],[6,3]\}$ is stabilized by h_{51+62}, h_{52+61}, and $\{h_{53},h_{63}\}$. Again, the terms h_{51+62} and h_{52+61} contribute with a large value to $\hat{F}_C$. On the other hand, the terms $\{h_{53},h_{63}\}$ contribute only moderately. This analysis suggests that the $\{[5,3],[6,3]\}$ channel should be the one driving the superconducting instability in the E_g channel and can be stabilized by large terms $\{h_{53},h_{63}\}$.

From this analysis, we can understand the tendencies observed in the numerical results as follows: the order parameters in A_{1g}, in particular $[5,2]-[6,1]$, are strongly stabilized by atomic SOC, in particular by the term h_{52-61} in the normal-state Hamiltonian, such that reducing the magnitude of this coupling is expected to weaken the superconducting instability in this channel. Moreover, the terms $\{h_{53},h_{63}\}$ primarily suppress the order parameter in this channel since their contribution to $\hat{F}_C$ is larger than the one to $\hat{F}_A$. In contrast, the E_g order parameters, in particular for $\{[5,3],[6,3]\}$, are primarily stabilized by $\{h_{53},h_{63}\}$ since for these terms the contribution to $\hat{F}_A$ is larger than the one to $\hat{F}_C$, while atomic SOC is clearly detrimental. This analysis suggests that by reducing the atomic SOC and enhancing the terms $\{h_{53},h_{63}\}$ associated with nonlocal SOC even in momentum, the ground state should change from A_{1g} to E_g.

8

Irrep	[a,b]	Interac.	h_{80}	h_{43}	h_{52-61}	h_{51+62}	h_{70}	h_{52+61}	h_{10}	h_{51-62}	h_{20}	h_{30}	h_{41}	h_{42}	h_{53}	h_{63}
A_{1g}	$[0,0]$	$U+2J'$	0	0	0	0	0	0	0	0	0	0	0	0	0	0
	$[8,0]$	$U-J'$	0	0	24	48	0	48	0	24	12	12	0	0	12	12
	$[4,3]$	$U'-J$	0	0	8	16	16	16	16	8	4	4	16	16	4	4
	$[5,2]-[6,1]$	$U'-J$	11	3	0	32	3	32	3	8	8	8	4	4	8	8
A_{2g}	$[5,1]+[6,2]$	$U'-J$	11	3	24	8	3	8	3	8	8	8	4	4	8	8
B_{1g}	$[7,0]$	$U-J'$	0	16	8	16	0	16	16	8	4	4	16	16	4	4
	$[5,2]+[6,1]$	$U'-J$	11	3	8	8	3	8	3	24	8	8	4	4	8	8
B_{2g}	$[1,0]$	$U'+J$	0	16	8	16	16	16	0	8	4	4	16	16	4	4
	$[5,1]-[6,2]$	$U'-J$	11	3	8	32	3	32	3	0	8	8	4	4	8	8
E_g	$+[3,0]$	$U'+J$	12	4	20	40	4	40	4	20	4	0	4	4	4	16
	$-[2,0]$		12	4	20	40	4	40	4	20	0	4	4	4	16	4
E_g	$+[4,2]$	$U'-J$	0	16	8	16	16	16	16	8	4	4	16	0	4	4
	$-[4,1]$		0	16	8	16	16	16	16	8	4	4	0	16	4	4
E_g	$+[5,3]$	$U'-J$	12	4	20	40	4	40	4	20	16	4	4	4	0	4
	$+[6,3]$		12	4	20	40	4	40	4	20	4	16	4	4	4	0

TABLE IV. Superconducting-fitness measure $\hat{F}_C$ for the 3D three-orbital model for Sr_2RuO_4. The same notation as in Table III has been used.

Effective two-orbital model in the $k_x k_z$-plane

Sufficiently far from the Brillouin-zone diagonals $k_y = \pm k_x$, the bands close to the Fermi energy are dominated by only two of the Ru d-orbitals. For concreteness, here we consider the $k_x k_z$-plane, but our conclusions remain qualitatively valid for general $\boldsymbol{k}$, except close to $k_y = \pm k_x$.

In the $k_x k_z$-plane, the dominant orbitals at the Fermi energy are d_{xz} and d_{xy}. Projecting into this subspace, we obtain an effective two-orbital Hamiltonian which is parametrized by

$$\hat{H}_{2\,\text{orb}}(\boldsymbol{k}) = \tilde{h}_{ab}(\boldsymbol{k})\,\tau_a \otimes \sigma_b, \tag{26}$$

where the $\tilde{h}_{ab}(\boldsymbol{k})$ are real functions of momentum, τ_a and σ_b are Pauli matrices for $a, b = 1, 2, 3$ and the 2×2 identity matrix for $a, b = 0$, encoding the orbital and the spin DOF, respectively. There are, in principle, 16 parameters $\tilde{h}_{ab}(\boldsymbol{k})$ but in the presence of time-reversal and inversion symmetries these are constrained to only six, including the term proportional to the identity. The symmetry-allowed terms are listed in Table V; we classify them in terms of the irreps of D_{2h}, which is the little group for D_{4h} in the $k_x k_z$-plane. Analogously, we can parametrize the s-wave gap matrices in the orbital basis as

$$\hat{\Delta} = d_0\,\tau_a \otimes \sigma_b\,(i\sigma_2). \tag{27}$$

The irreps associated with each $[a,b]$ combination are the same as for the normal-state Hamiltonian, given in the first two columns of Table V.

The superconducting-fitness analysis, which is summarized in Table VI, is very much simplified in the two-orbital scenario since the symmetry-allowed matrices form a totally anticommuting set. From the table, one can see that the results concerning $\hat{F}_A(\boldsymbol{k})$ and $\hat{F}_C(\boldsymbol{k})$ are complementary. Note that the trivial order parameter, $[0,0]$, is stabilized by all the terms in the Hamiltonian while the remaining order parameters of the form $[a,b]$ need the associated term $\tilde{h}_{ab}$ in the Hamiltonian to develop a weak-coupling instability. There is an attractive interaction in the orbital-singlet spin-triplet channels $[2,b]$. The order parameter $[2,1]$ in A_g is stabilized by the atomic SOC term $\tilde{h}_{21}$. The other two potentially attractive channels $[2,2]$ in B_{1g} and $[2,3]$ in B_{2g} are stabilized by $\tilde{h}_{22}$ and $\tilde{h}_{23}$, respectively. Note, however, that $\tilde{h}_{22}$ is zero in the $k_x k_z$-plane (also also in the equivalent $k_y k_z$-plane), which should significantly reduce the stability of this state. We are then left with $[2,1]$ in A_g and $[2,3]$ in B_{2g} as good candidates: For strong atomic SOC $\tilde{h}_{21}$, the A_g channel should be the most stable, whereas for $\tilde{h}_{23} > \tilde{h}_{21}$, the B_{2g} channel becomes the most robust.

We now connect this discussion with the results of the three-orbital analysis above. The order parameter $[2,1]$ in the two-orbital model corresponds to both $[5,2]-[6,1]$ in A_{1g} and $[5,2]+[6,1]$ in B_{1g} of the three-orbital model,

Irrep	(a,b)	Type	Basis	Value in $k_x k_z$-plane	Three-orbital model
	$(0,0)$	intra-orbital hopping			$(0,0)$ in A_{1g}
A_g	$(3,0)$	intra-orbital hopping	$1, x^2, y^2, z^2$	finite	$(8,0)$ in A_{1g}
	$(2,1)$	atomic SOC			$(6,1)$ in A_{1g}/B_{1g}
B_{1g}	$(2,2)$	$\boldsymbol{k}$-SOC	xy	0	$(6,2)$ in A_{2g}/B_{2g}
B_{2g}	$(2,3)$	$\boldsymbol{k}$-SOC	xz	finite	$(6,3)$ in E_g
B_{3g}	$(1,0)$	inter-orbital hopping	yz	0	$(3,0)$ in E_g

TABLE V. List of the six symmetry-allowed terms in the effective two-orbital normal-state Hamiltonian $\hat{H}_{2\,\mathrm{orb}}(\boldsymbol{k})$ given by Eq. (26). For each (a,b), the basis function $\tilde{h}_{ab}(\boldsymbol{k})$ should transform according to a specific irrep of D_{2h} and can be associated with different physical processes ("Type"). The table also gives associated basis functions and provides information on whether they are finite or zero in the $k_x k_z$-plane and on the associated term in the original three-orbital model.

			$\hat{F}_A$					$\hat{F}_C$				
			A_g	B_{1g}	B_{2g}	B_{3g}		A_g	B_{1g}	B_{2g}	B_{3g}	
Irrep	$[a,b]$	Interac.	$\boldsymbol{\tilde{h}_{30}}$	$\boldsymbol{\tilde{h}_{21}}$	$\tilde{h}_{22}$	$\tilde{h}_{23}$	$\tilde{h}_{10}$	$\boldsymbol{\tilde{h}_{30}}$	$\boldsymbol{\tilde{h}_{21}}$	$\tilde{h}_{22}$	$\tilde{h}_{23}$	$\tilde{h}_{10}$
	$[0,0]$	$U+2J'$	1	1	1	1	1	0	0	0	0	0
A_g	$[3,0]$	$U-J'$	1	0	0	0	0	0	1	1	1	1
	$[2,1]$	$\boldsymbol{U'-J}$	0	1	0	0	0	1	0	1	1	1
B_{1g}	$[2,2]$	$\boldsymbol{U'-J}$	0	0	1	0	0	1	1	0	1	1
B_{2g}	$[2,3]$	$\boldsymbol{U'-J}$	0	0	0	1	0	1	1	1	0	1
B_{3g}	$[1,0]$	$U'+J$	0	0	0	0	1	1	1	1	1	0

TABLE VI. Superconducting-fitness analysis for the effective two-orbital model in the $k_x k_z$-plane. The first column gives the irrep of D_{2h} of the order parameter parametrized by the matrices $[a,b]$ (second column), the third column displays the local interaction in the respective channel, where the potentially attractive channels are highlighted in boldface. Columns 4–8 give the results for the fitness function $\hat{F}_A$ such that $\mathrm{Tr}\,\hat{F}_A^\dagger(\boldsymbol{k})\hat{F}_A(\boldsymbol{k}) = \sum_{cd}(\text{table entry})\,|\tilde{h}_{cd}(\boldsymbol{k})|^2$, for each term $[c,d]$ in the normal-state Hamiltonian. Analogously, columns 9–13 give the results for the fitness function $\hat{F}_C$. We highlight in boldface the $\tilde{h}_{cd}$ terms which are usually present in 2D models, while the terms in normal typeface describe momentum-dependent SOC or interlayer hopping.

whereas $[2,3]$ in the two-orbital model corresponds to $\{[5,3],[6,3]\}$ in E_g. As discussed in the main text, the leading pairing instabilities are in the E_g and A_{1g} channels, whereas the B_{1g} channel is the subleading instability over much of the region where the A_{1g} channel is dominant. The fact that the B_{1g} channel is a subleading instability is not surprising, since it must go through a zero as one moves along the Fermi surface from the $k_x k_z$- to the $k_y k_z$-plane, whereas the A_{1g} channel maintains a full gap. Since the attractive interactions in both channels are the same, the A_{1g} state will be favored over B_{1g}.

The fact that atomic SOC favors the A_{1g} channel, while increasing the $\{h_{53}, h_{63}\}$ terms can stabilize an E_g state, is consistent with the numerical analysis presented in the main text. A naive interpretation of the two-orbital model implies that the E_g state is stabilized over the A_{1g} when $\tilde{h}_{23} > \tilde{h}_{21}$. However, we numerically find in the full three-orbital model that the condition is closer to $\{h_{53}, h_{63}\} \gtrsim h_{52-61}/4$. This discrepancy reflects the fact that the two-orbital model is not valid over the entire Brillouin zone. Nevertheless, the two-orbital model accurately identifies the terms which stabilize the E_g state over the A_{1g}.

[S1] C. N. Veenstra, Z.-H. Zhu, M. Raichle, B. M. Ludbrook, A. Nicolaou, B. Slomski, G. Landolt, S. Kittaka, Y. Maeno, J. H. Dil, I. S. Elfimov, M. W. Haverkort, and A. Damascelli, Spin-Orbital Entanglement and the Breakdown of Singlets and Triplets in Sr$_2$RuO$_4$ Revealed by Spin- and Angle-Resolved Photoemission Spectroscopy, Phys. Rev. Lett. **112**, 127002 (2014).
[S2] M. Gradhand, K. I. Wysokinski, J. F. Annett, and B. L. Györffy, Kerr rotation in the unconventional superconductor Sr$_2$RuO$_4$, Phys. Rev. B **88**, 094504 (2013).
[S3] T. Scaffidi, J. C. Romers, and S. H. Simon, Pairing symmetry and dominant band in Sr$_2$RuO$_4$, Phys. Rev. B **89**, 220510(R)

(2014).

[S4] W. Huang and H. Yao, Possible Three-Dimensional Nematic Odd-Parity Superconductivity in Sr_2RuO_4, Phys. Rev. Lett. **121**, 157002 (2018).

[S5] D. E. King, Dlib-ml: A Machine Learning Toolkit, J. Machine Learning Research **10**, 1755 (2009).

[S6] A. Ramires and M. Sigrist, Identifying detrimental effects for multi-orbital superconductivity: Application to Sr_2RuO_4, Phys. Rev. B **94**, 104501 (2016).

[S7] A. Ramires, D. F. Agterberg, and M. Sigrist, Tailoring T_c by symmetry principles: The concept of superconducting fitness, Phys. Rev. B **98**, 024501 (2018).